1   **Chapter 6: Paleoclimate**
2   **Figures**
3
4   **Coordinating Lead Authors:**
5   Eystein Jansen (Norway), Jonathan Overpeck (USA)
6
7   **Lead Authors:**
8   Keith R. Briffa (UK), Jean-Claude Duplessy (France), Fortunat Joos (Switzerland), Valérie Masson-
9   Delmotte (France), Daniel O. Olago (Kenya), Bette Otto-Bliesner (USA), Wm. Richard Peltier (Canada),
10   Stefan Rahmstorf (Germany), Rengaswamy Ramesh (India), Dominique Raynaud (France), David H. Rind
11   (USA), Olga Solomina (Russia), Ricardo Villalba (Argentina), De'er Zhang (China).
12
13   **Contributing Authors:**
14   Jean-Marc Barnola (France), Eva Bauer (Germany), Esther Brady (USA), Mark Chandler (USA), Julia Cole
15   (USA), Edward R. Cook (USA), Elsa Cortijo (France), Trond Dokken (Norway), Dominik Fleitmann (USA),
16   Zhengtang Guo (China), Masa Kageyama ((France), Myriam Khodri (USA), Laurent Labeyrie (France),
17   Alexandre Laîné (France), Anders Levermann (Germany), Øyvind Lie (Norway), Marie-France Loutre
18   (Belgium), Katsumi Matsumoto (USA), Erik Monnin (Switzerland), Daniel Muhs (USA), Raimund
19   Muscheler (USA, Germany), Timothy J. Osborn (UK), Øyvind Paasche (Norway), Frederic Parrenin
20   (France), Gian-Kasper Plattner(Switzerland), Henry N. Pollack (USA), Lowell Stott (USA), Ellen Mosley-
21   Thompson (USA), Renato Spahni (Switzerland), Lonnie Thompson (USA), Claire Waelbroeck (France),
22   Gregory Wiles (USA), Jim Zachos (USA).
23
24   **Review Editors:** Jean Jouzel (France), John Mitchell (UK)
25
26   **Date of Draft:** 27 October 2006
27
28

1
2
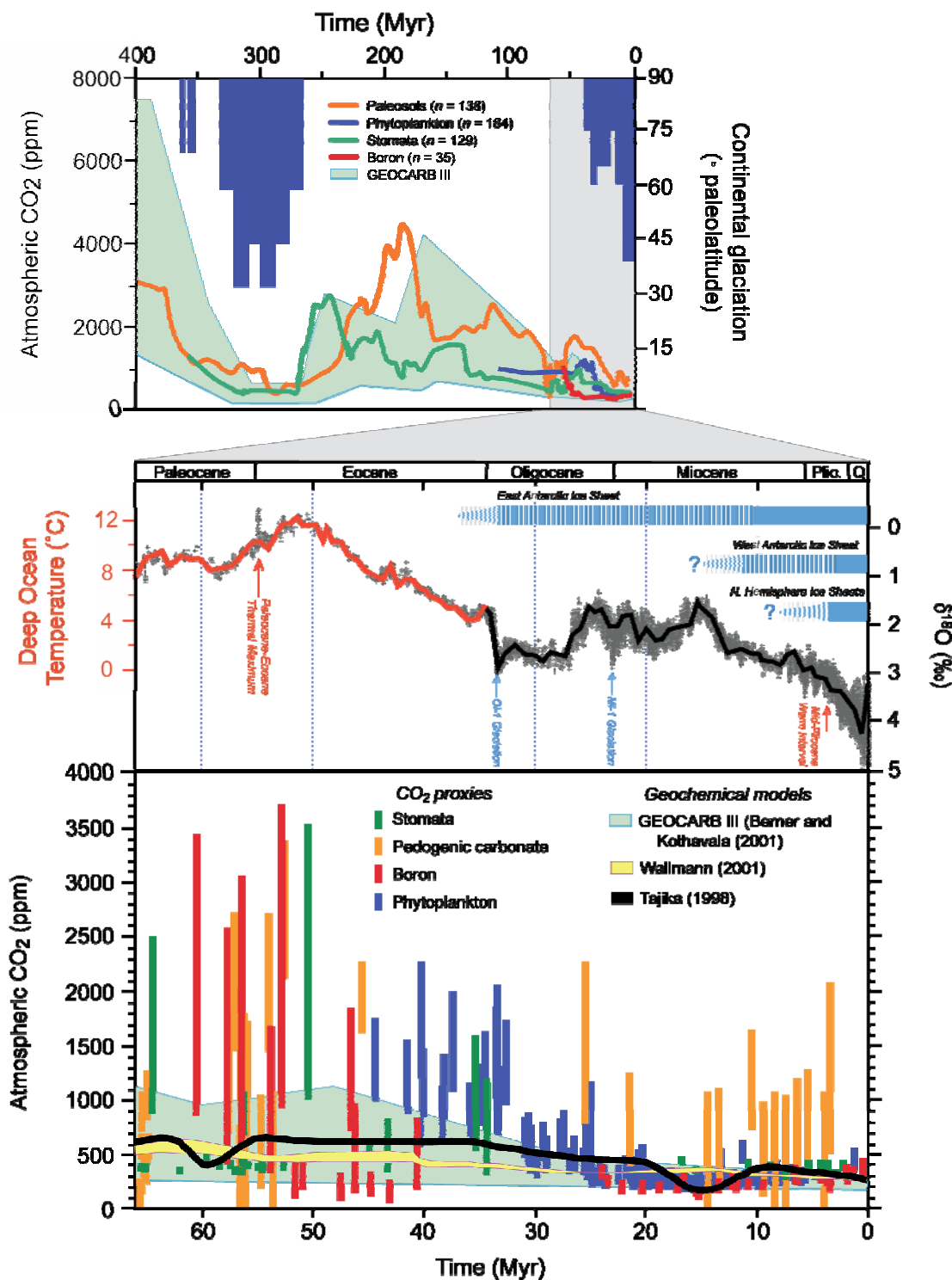
3
4
Figure 6.1. <u>Top panel</u>: Atmospheric CO_2 and continental glaciation 400 Myr ago to present. Vertical blue
bars mark the timing and paleolatitudinal extent of ice sheets (after Crowley, 1998). Plotted CO_2 records
represent five-point running averages from each of the four major proxies (see Royer, 2006 for details of
compilation). Also plotted are the plausible ranges of CO_2 from the geochemical carbon cycle model
GEOCARB III (Berner and Kothavala, 2001). All data have been adjusted to the Gradstein et al. (2004)
timescale. <u>Middle panel</u>: Global compilation of deep-sea benthic foraminifera oxygen isotope records from
40 DSDP and ODP sites (Zachos et al., 2001) updated with high-resolution records for the Eocene through
Miocene interval (Billups et al., 2002; Bohaty and Zachos, 2003; Lear et al., 2004). Most data were derived
from analyses of two common and long-lived benthic taxa, *Cibicidoides* and *Nuttallides*. To correct for
genus-specific isotope vital effects, the ^{18}O values were adjusted by +0.64 and +0.4 (Shackleton et al., 1984),

1   respectively. The ages are relative to the GPTS of Berggren et al. (1995). The raw data were smoothed using
2   a five-point running mean, and curve-fitted with a locally weighted mean. The ^{18}O temperature values
3   assume an ice-free ocean [-1.0‰ Standard Mean Ocean Water (SMOW)], and thus only apply to the time
4   preceding large-scale Antarctica glaciation (~35 Myr ago). After early Oligocene much of the variability
5   (~70%) in the ^{18}O record reflects changes in Antarctica and Northern Hemisphere ice volume, which is
6   represented by light blue, horizontal bars (e.g., Hambrey et al., 1991; Wise et al., 1991; Ehrmann and
7   Mackensen, 1992). Where the bars are dashed they represent periods of ephemeral ice or ice-sheets smaller
8   than present, while the solid bars represent ice sheets of modern or greater size. The evolution and stability
9   of the West Antarctic ice sheet (e.g., Lemasurier and Rocchi, 2005) remains an important area of uncertainty
10 that could impact estimates of future sea level rise. <u>Bottom panel</u>: Detailed record of CO_2 for the last 65 Myr.
11 Individual records of CO_2 and associated errors are color-coded by proxy method; when possible, records are
12 based on replicate samples (see Royer, 2006 for details). Dating errors are typically $<\pm1$ Myr. The range of
13 error for each CO_2 proxy varies considerably with estimates based on soil nodules yielding the greatest
14 uncertainty. Also plotted are the plausible ranges of CO_2 from three geochemical carbon cycle models.
15

1
2
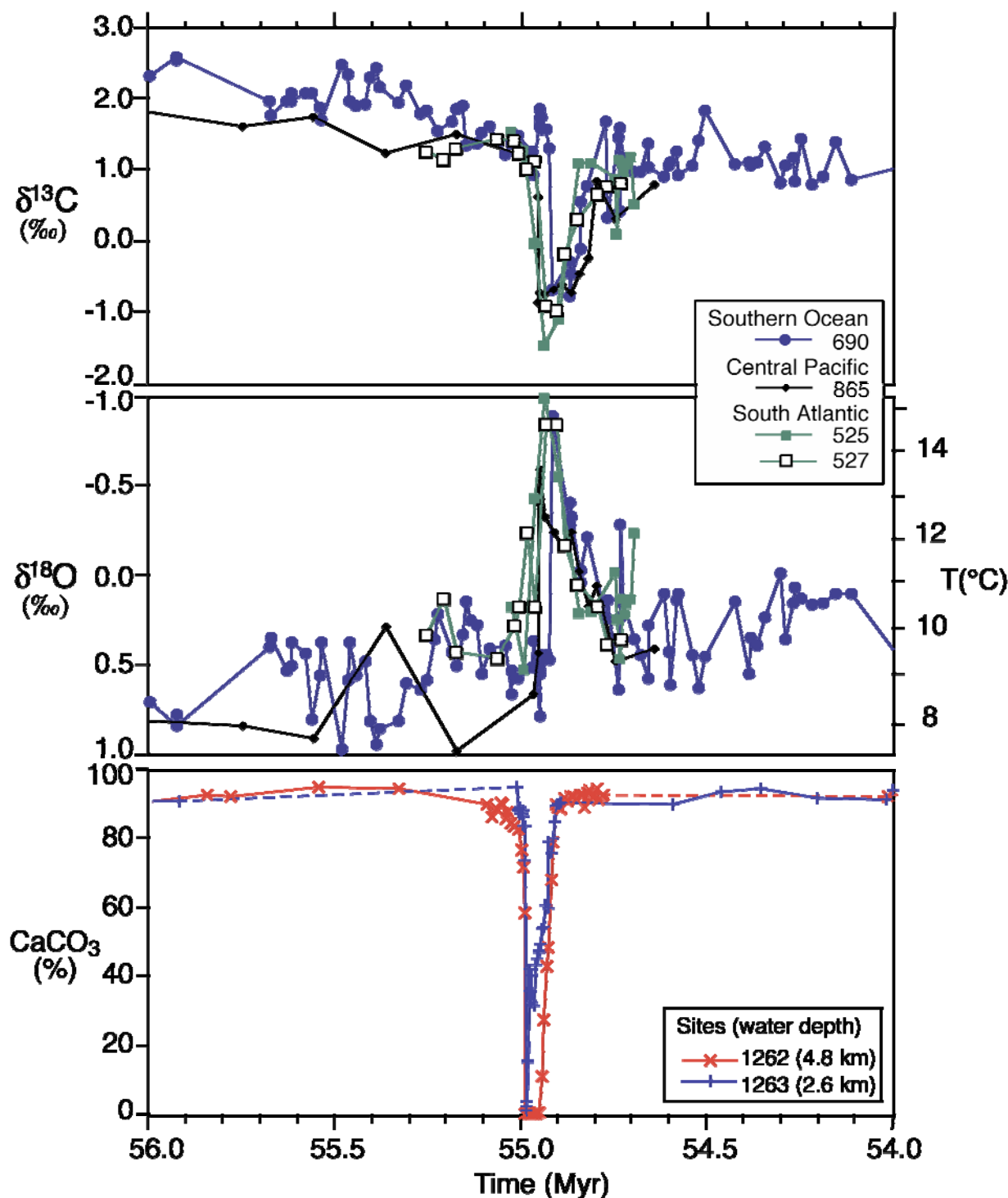
3
4
5   **Figure 6.2.** The Paleocene-Eocene Thermal Maximum (PETM) as recorded in benthic (bottom dwelling)
6   foraminifer (*N. truempyi*) isotopic records from sites in the Antarctic, south Atlantic and Pacific (see Zachos
7   et al., 2003 for details). The rapid decrease in carbon isotope ratios in the top panel is indicative of a large
8   increase in atmospheric greenhouse CO_2 and CH_4, that was coincident with ~5°C global warming (center
9   panel). Using the carbon isotope records, numerical models show that CH_4 released by the rapid
10   decomposition of marine hydrates might have been a major component (~2000 GtC) of the carbon flux
11   (Dickens and Owen, 1996). Testing of this and other models requires an independent constraint on the
12   carbon fluxes. In theory, the much of the additional greenhouse carbon would have been absorbed by the
13   ocean, thereby lowering seawater pH and causing widespread dissolution of seafloor carbonates. Such a
14   response is evident in the lower panel which shows a transient reduction in the carbonate content of
15   sediments in two cores from the south Atlantic (Zachos et al., 2004; Zachos et al., 2005). The observed

1   patterns indicate that the oceans carbonate saturation horizon rapidly shoaled over 2 km, and then gradually
2   recovered as buffering processes slowly restored the chemical balance of the ocean. Initially, most of the
3   carbonate dissolution is of sediment deposited prior to the event, a process that offsets the apparent timing of
4   the dissolution horizon relative to the base of the benthic foraminifer carbon isotope excursion. Model
5   simulations show that the recovery of the carbonate saturation horizon should precede the recovery in the
6   carbon isotopes by as much as 100 kyr (Dickens and Owen, 1996), another feature that is evident in the
7   sediment records.
8

1
2
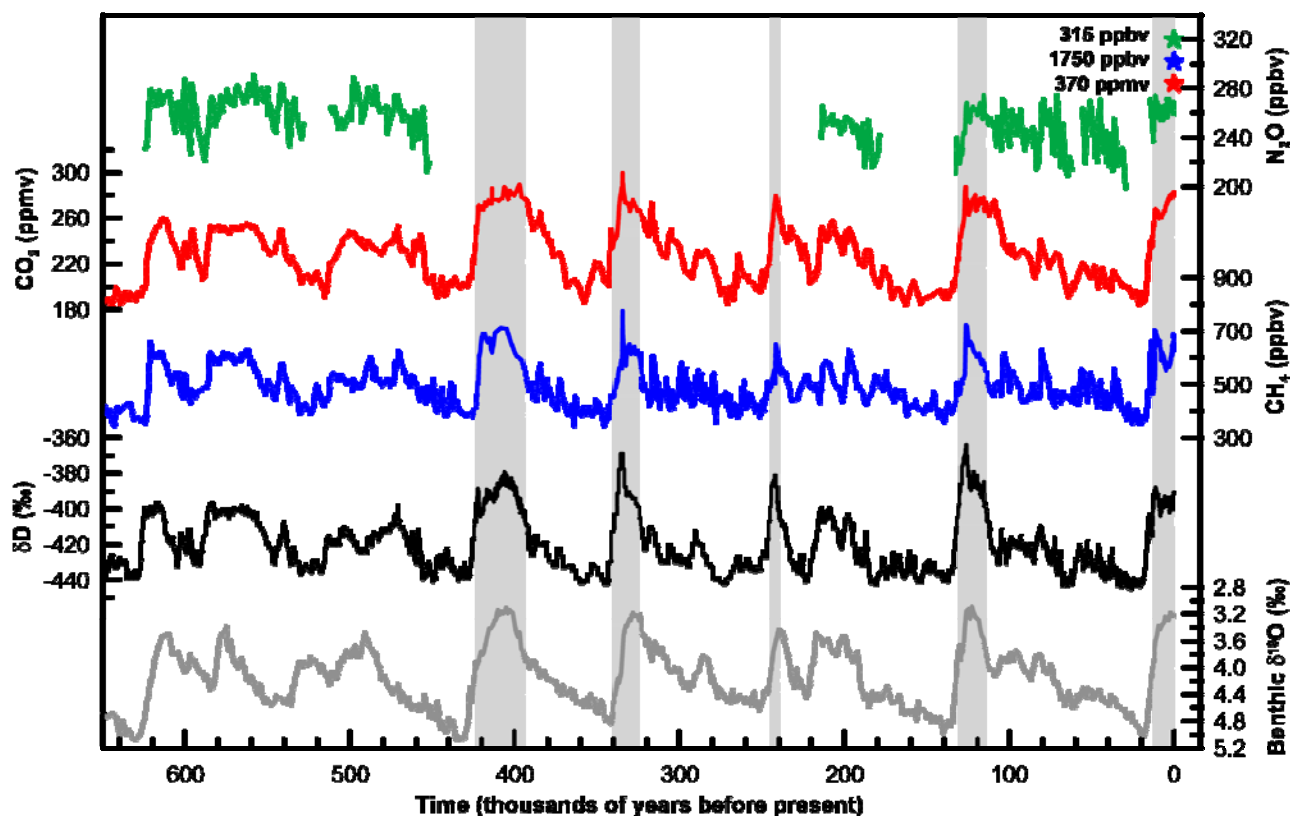
3
4
Figure 6.3. Variations of deuterium (δD), a proxy for local temperature, and the atmospheric concentrations
of the greenhouse gases carbon dioxide, methane, and nitrous oxide derived from air trapped within ice cores
from Antarctica and from recent atmospheric measurements (Petit et al., 1999; Indermühle et al., 2000;
EPICA community members, 2004; Spahni et al., 2005; Siegenthaler et al., 2005ab). The shading indicates
the last interglacial warm periods. Interglacial periods also existed prior to 450,000 years, but these were
apparently colder than the typical interglacials of the latest Quaternary. The length of the current interglacial
is, in the context of the last 650,000 years, not unusual. The stack of 57 globally distributed benthic $\delta^{18}O$
marine records, a proxy for global ice volume fluctuations (Lisiecki and Raymo, 2005), is displayed in the
bottom part of the figure for comparison with the ice core data. Larger ice volume is expressed downwards.
Note that the shaded vertical bars are based on the ice core age model (EPICA community members, 2004),
and that the marine record is plotted on its original time scale based on tuning to the orbital parameters
(Lisiecki and Raymo, 2005). The stars and labels indicate concentrations at year 2000.
17

1
2
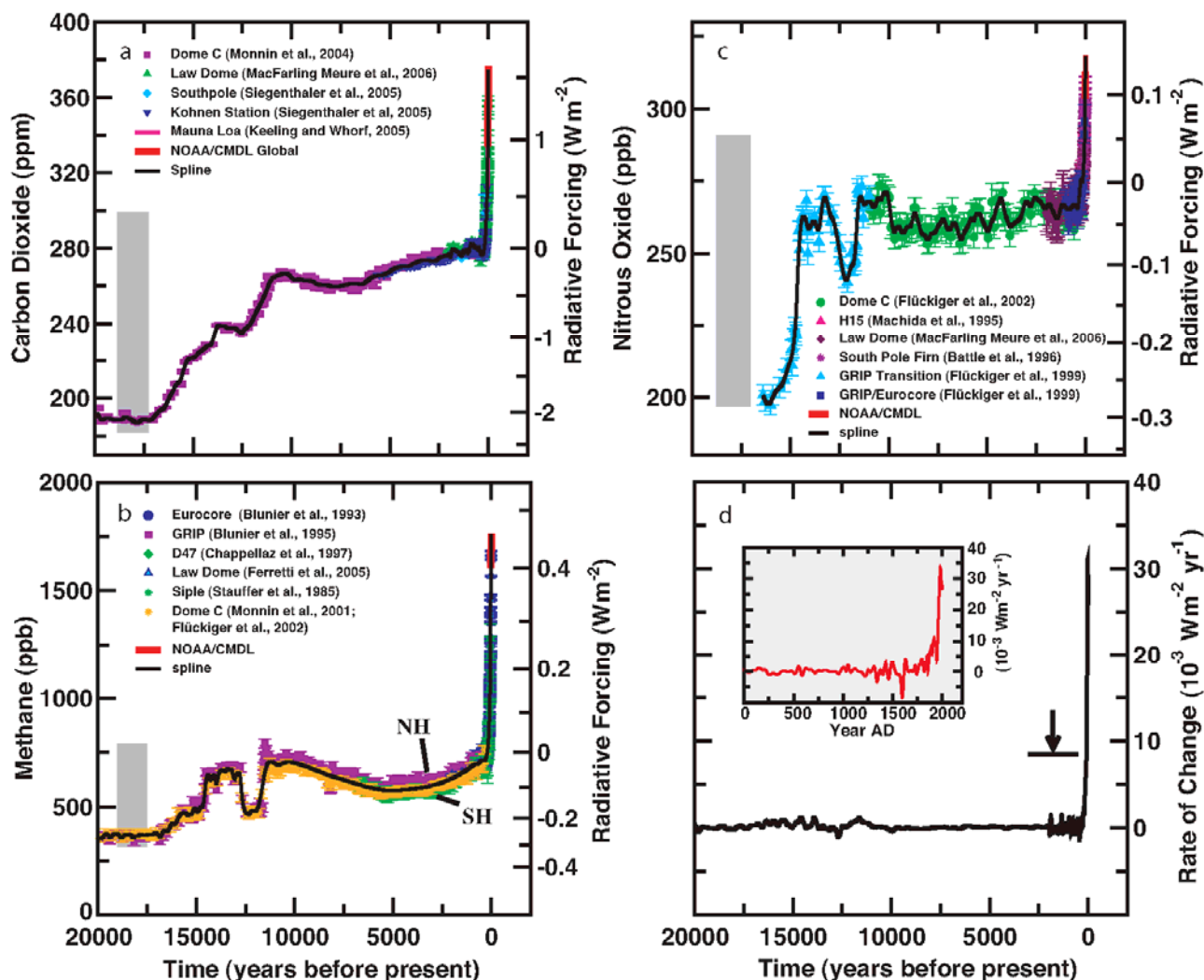
3
4
5
6   **Figure 6.4.** The concentrations and radiative forcing by (a) carbon dioxide (CO_2), (b) methane (CH_4), (c)
7   nitrous oxide (N_2O), and (d) the rate of change in their combined radiative forcing over the last 20,000 years
8   reconstructed from Antarctic and Greenland ice and firn data (symbols) and direct atmospheric
9   measurements (red and magenta lines). The grey bars show the reconstructed ranges of natural variability for
10   the past 650,000 years (Siegenthaler et al., 2005a; Spahni et al., 2005). Radiative forcing has been computed
11   with the simplified expressions of chapter 2 (Myhre et al., 1998). The rate of change in radiative forcing
12   (black line) has been computed from spline fits (Enting, 1987) of the concentration data (black lines in panel
13   a-c). The width of the age distribution of the bubbles in ice varies from ~20 years for sites with a high
14   accumulation of snow such as Law Dome, Antarctica, to ~200 years for low accumulation sites such as
15   Dome C, Antarctica. The Law Dome ice and firn data, covering the past two millennia, and recent
16   instrumental data have been splined with a cut-off period of 40 years, with the resulting rate of change in
17   radiative forcing is shown by the inset in d. The arrow shows the peak in the rate of change in radiative
18   forcing after the anthropogenic signals of CO_2, CH_4, and N_2O have been smoothed with a model describing
19   the enclosure process of air in ice (Spahni et al., 2003) applied for conditions at the low accumulation Dome
20   C site for the last glacial transition. The CO_2 data are from (Etheridge et al., 1996; Monnin et al., 2001;
21   MacFarling Meure et al., 2006; Monnin et al., 2004; Siegenthaler et al., 2005b [Southpole]; Siegenthaler et
22   al., 2005a [Kohnen Station]), the CH_4 data from (Stauffer et al., 1985; Steele et al., 1992; Blunier et al.,
23   1993; Dlugokencky et al., 1994; Blunier et al., 1995; Chappellaz et al., 1997; Monnin et al., 2001; Flückiger
24   et al., 2002; Ferretti et al., 2005), the N_2O data from (Machida et al., 1995; Battle et al., 1996; Flückiger et
25   al., 1999; Flückiger et al., 2002; MacFarling Meure et al., 2006). Atmospheric data are from the NOAA
26   global air sampling network, representing global average concentrations (dry air mole fraction) (Steele et al.,

1 1992; Dlugokencky et al., 1994; Tans and Conway, 2005), and from Mauna Loa, Hawaii (Keeling and
2 Whorf, 2005). The globally averaged data are available from: http://www.cmdl.noaa.gov/.
3

1
2
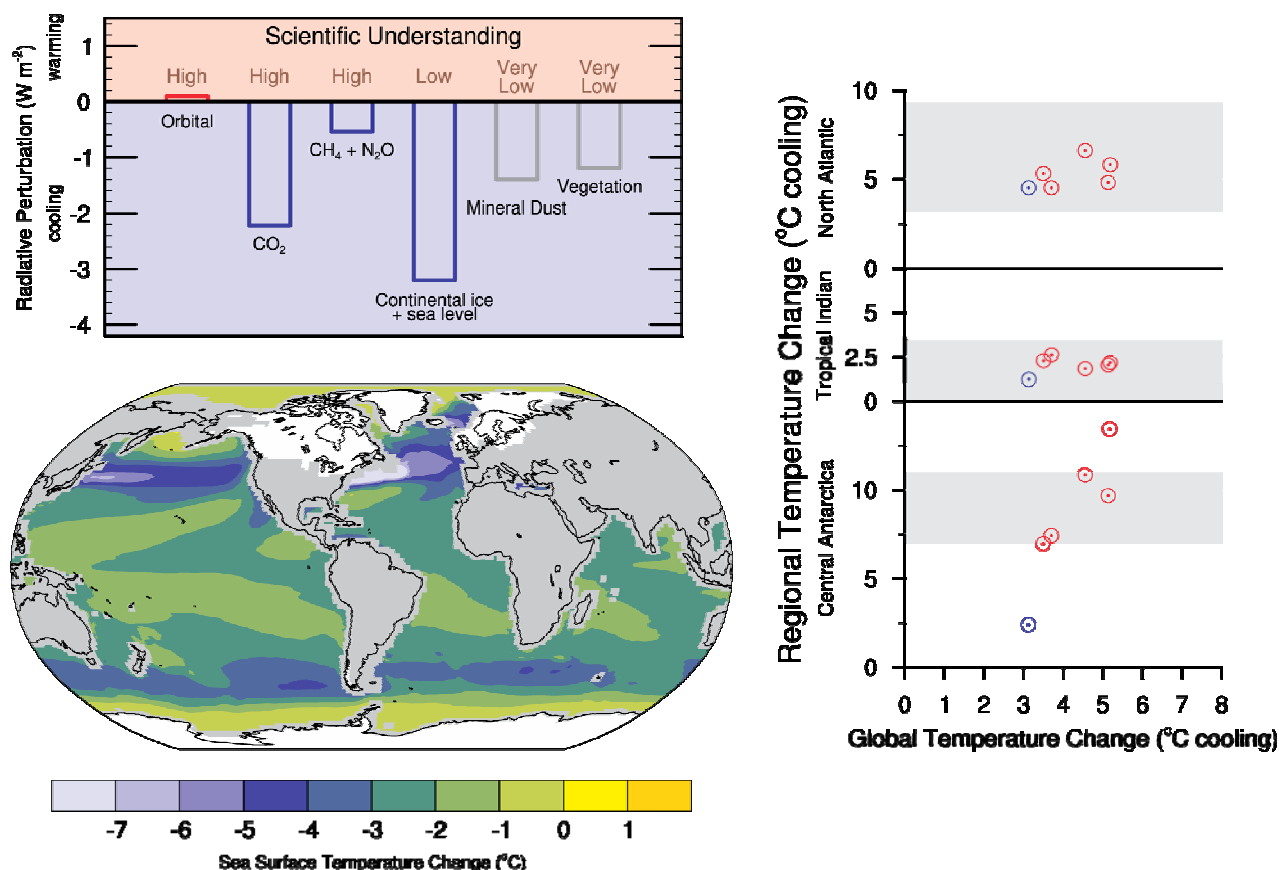
3
4
5
6 **Figure 6.5.** The Last Glacial Maximum climate (approximately 21kyrs ago) relative to pre-industrial (1750).
7 Top left: Global annual mean radiative influences (W m^{-2}) of LGM climate change agents, generally
8 feedbacks on glacial-interglacial cycles, but also specified in most AOGCM simulations for LGM. The
9 heights of the rectangular bars denote best estimate values guided by published values of the climate change
10 agents and conversion to radiative perturbations using simplified expressions for the greenhouse gas
11 concentrations and model calculations for the ice sheets, vegetation, and mineral dust. References are
12 included in text. A judgment of the each estimate's reliability is given as a level of scientific understanding
13 based on uncertainties in the climate change agents and our physical understanding of their radiative effects.
14 PMIP-2 simulations shown in bottom left and right panels do not include the radiative influences of LGM
15 changes in mineral dust or vegetation. Bottom left: Multi-model average SST change for LGM PMIP-2
16 simulations by five AOGCMs (CCSM, FGOALS, HadCM, IPSL, and MIROC). Ice extent over continents is
17 shown in white. Right: LGM regional cooling as compared to LGM global cooling as simulated in PMIP-2,
18 AOGCM results shown as red circles, EMIC (ECBilt-CLIO) result shown as blue circle. Regional averages
19 are defined as Antarctica, annual for inland ice cores; tropical Indian Ocean, annual for 15°S–15°N, 50–
20 100°E; North Atlantic Ocean, July-August-September for 42–57°N, 35°W–20°E. Grey shading indicates
21 range of observed proxy estimates of regional cooling: Antarctica (Stenni et al., 2001; Masson-Delmotte et
22 al., 2006), tropical Indian Ocean (Rosell-Mele et al., 2004; Barrows and Juggins, 2005), North Atlantic
23 Ocean (Rosell-Mele et al., 2004; deVernal et al., 2006; Kucera et al., 2005; Kageyama et al., 2006).
24

1
2
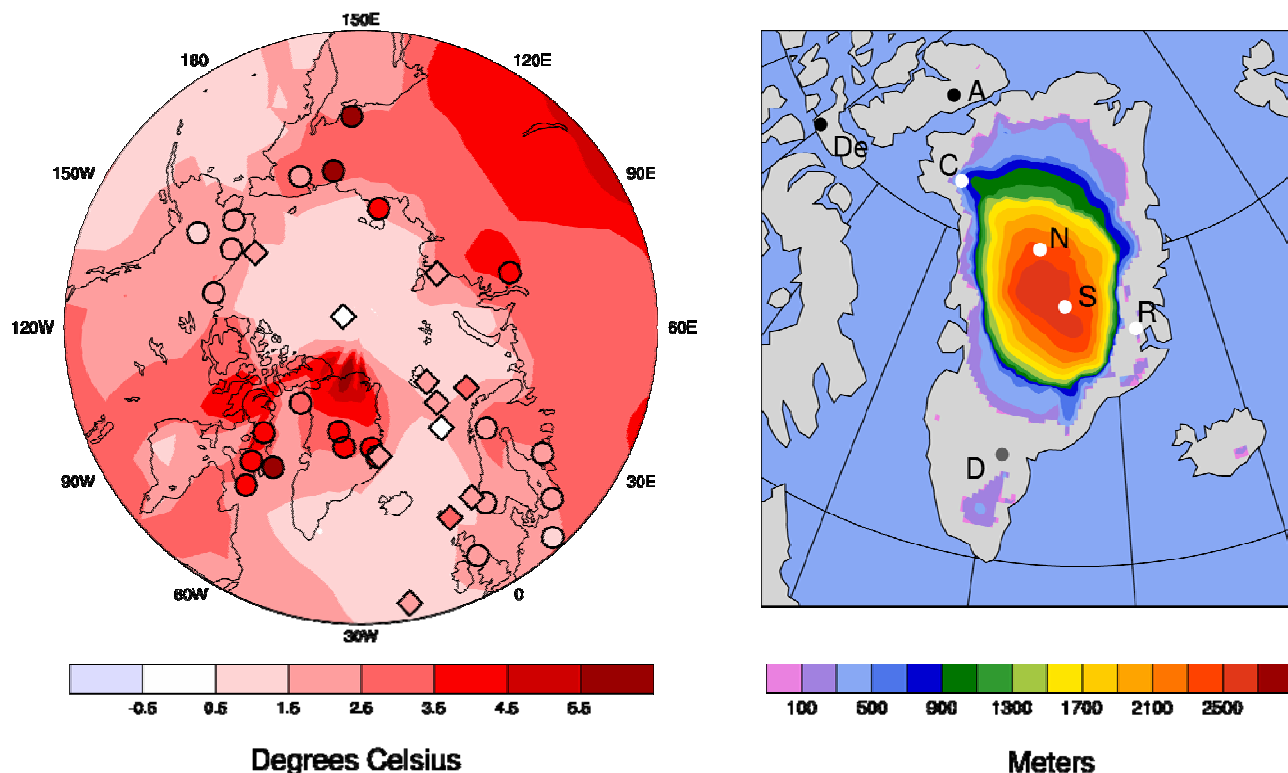
Figure 6.6. Summer surface air temperature change over the Arctic, as well as annual ice thickness and extent for Greenland and western Arctic glaciers, for the Last Interglacial (LIG) at approximately 130–125 kyr ago from a multi-model and a multi-proxy synthesis. The multi-model summer warming simulated by the NCAR CCSM, 130 kyr ago minus present (Otto-Bliesner et al., 2006a) and ECHO-G model, 125 kyr ago minus preindustrial (Kaspar et al., 2005) is contoured in the left panel and is overlain by proxy estimates of maximum summer warming from terrestrial (circles) and marine (diamonds) sites as compiled in the syntheses published by the CAPE Project Members (2006) and Kaspar et al. (2005). Extents and thicknesses of the Greenland Ice Sheet and eastern Canadian and Iceland glaciers are shown at their minimum extent for the LIG as a multi-model average from three ice models (Tarasov and Peltier, 2003; Lhomme et al., 2005a; Otto-Bliesner et al., 2006b). Ice core observations (Koerner, 1989; North Greenland Ice Core Project, 2004) indicate Last Interglacial ice (white dots) at Renland (R), NGRIP (N), Summit (S, GRIP and GISP2), and possibly Camp Century (C); no LIG ice (black dots) at Devon (De) and Agassiz (A) in the eastern Canadian Arctic. Evidence for LIG ice at Dye-3 in southern Greenland is equivocal (gray dot; see text for detail).

1
2
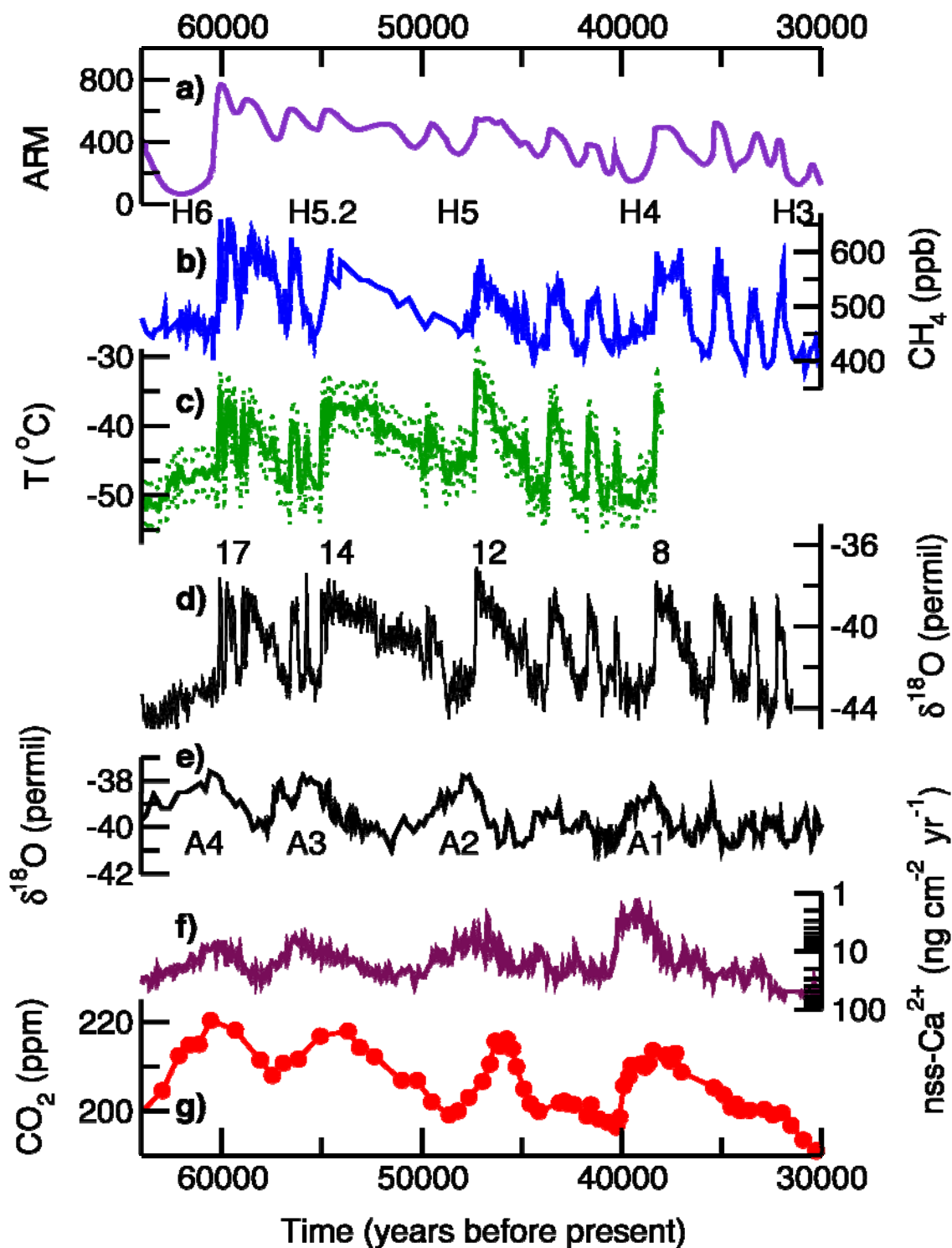
3
4
5 **Figure 6.7.** The evolution of climate indicators from the Northern Hemisphere (panels a to d), and from
6 Antarctica (panels e to g), over the period 64 to 30 kyr ago. a) Anhysteretic remanent magnetisation (ARM),
7 here a proxy of the northward extent of Atlantic Meridional Overturning circulation, from an ocean sediment
8 core from the Nordic Seas (Dokken and Jansen, 1999); b) methane as recorded in Greenland ice cores at the
9 GRIP, GISP and NorthGRIP sites (Blunier and Brook, 2001; Flückiger et al., 2004; Huber et al., 2006). CH_4
10 data for the period 40 to 30 kyr ago were selected for the GRIP site and for 64 to 40 kyr ago for the GISP site
11 when sample resolution is highest in the cores; c) surface temperature estimated from nitrogen isotope ratios
12 that are influenced by thermal diffusion (Huber et al., 2006); d) $\delta^{18}O$, a proxy for surface temperature, from
13 NorthGRIP (North Greenland Ice Core Project, 2004) with the Dansgaard-Oeschger Northern Hemisphere
14 warm events 8, 12, 14, and 17 indicated; e) $\delta^{18}O$ from Byrd, Antarctica (Blunier and Brook, 2001) with A1

1   to A4 denoting Antarctic warm events; f) nss-Ca^2-, a proxy of dust and iron deposition, from Dome C,
2   Antarctica (Röthlisberger et al., 2004); g) CO_2 as recorded in ice from Taylor Dome, Antarctica (Indermühle
3   et al., 2000). The Heinrich events, periods of massive ice rafted debris recorded in marine sediments, H3,
4   H4, H5, H5.2, and H6, are shown. All data are plotted on the Greenland SS09sea time scale (Johnsen et al.,
5   2001). CO_2 and CH_4 are well mixed in the atmosphere. CH_4 variations are synchronous within the resolution
6   of ±50 years with variations in Greenland temperature, but a detailed analysis suggests that CH_4 rises lag
7   temperature increases at the onset of the Dansgaard-Oeschger events by 25 to 70 year (Huber et al., 2006).
8   CO_2 co-varied with the Antarctic temperature, but the exact synchronisation between Taylor Dome and Byrd
9   is not without uncertainties, thus making the determination of lead or lags between temperature and CO_2
10 elusive. The evolution of Greenland and Antarctic temperature is consistent with a reorganisation of the heat
11 transport and the Meridional Overturning Circulation in the Atlantic (Knutti et al., 2004).
12

1
2
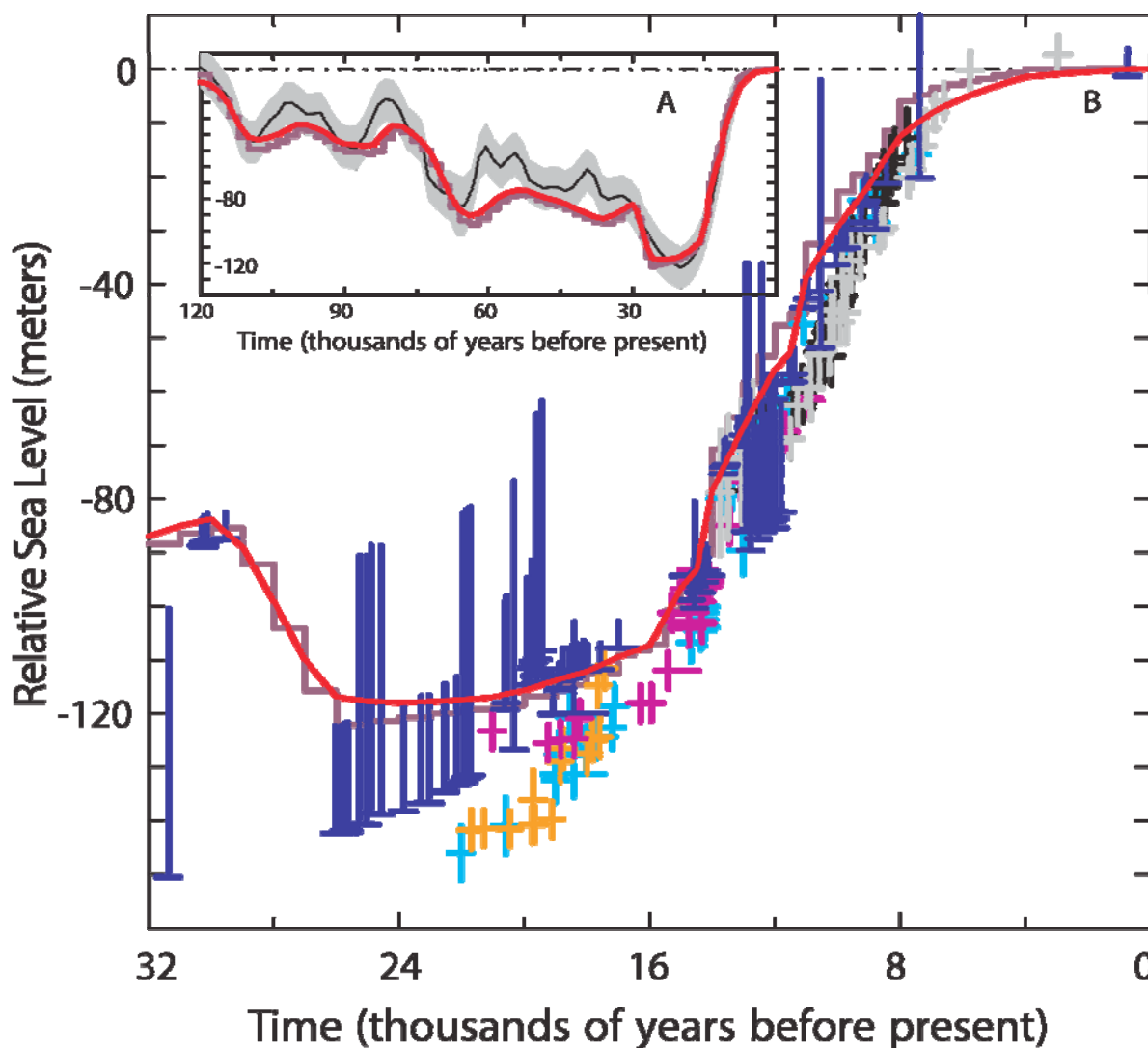
3
4
5 **Figure 6.8.** (a) The ice equivalent eustatic sea level history over the last glacial-interglacial cycle according
6 to the analysis of Waelbroeck et al. (2002). The smooth black line defines the mid-point of their estimates for
7 each age and the surrounding hatched region provides an estimate of error. The red line is the prediction of
8 the ICE-5G(VM2) model for the Barbados location for which the relative sea level observations themselves
9 provide an excellent approximation to the ice equivalent eustatic sea level curve. The actual ice equivalent
10 eustatic sea level curve for this model is shown as the step-discontinuous purple line. (b) The fit of the ICE-
11 5G(VM2) model prediction (red line) to the extended coral based record of relative sea level history from the
12 island of Barbados in the Caribbean Sea (Fairbanks, 1989; Peltier and Fairbanks, 2006) over the age range
13 from the present day to 32 ka to present. The individual coral based estimates of relative sea level (blue)
14 have an attached error bar that depends upon the coral species. The estimates denoted by the short error bars
15 are derived from the *Acropora Palmata* species which provide the tightest constraints upon relative sea level
16 as this species is found to live within approximately 5m of sea level in the modern ecology. The estimates
17 denoted by the longer error bars are derived either from the *Montastrea Annularis* species of coral (error bars
18 of intermediate 20 m length) or from further species which are found over a wide range of depths with
19 respect to sea level (longest error bars). These additional data are most useful in providing a lower bound for
20 the sea level depression. The data denoted by the colored crosses are from the ice equivalent eustatic sea
21 level reconstruction of Lambeck and Chappell (2001). The color code employed for these data is as follows:
22 cyan (Barbados), grey(Tahiti), black(Huon), orange(Bonaparte Gulf), purple(Sunda Shelf).
23

1
2
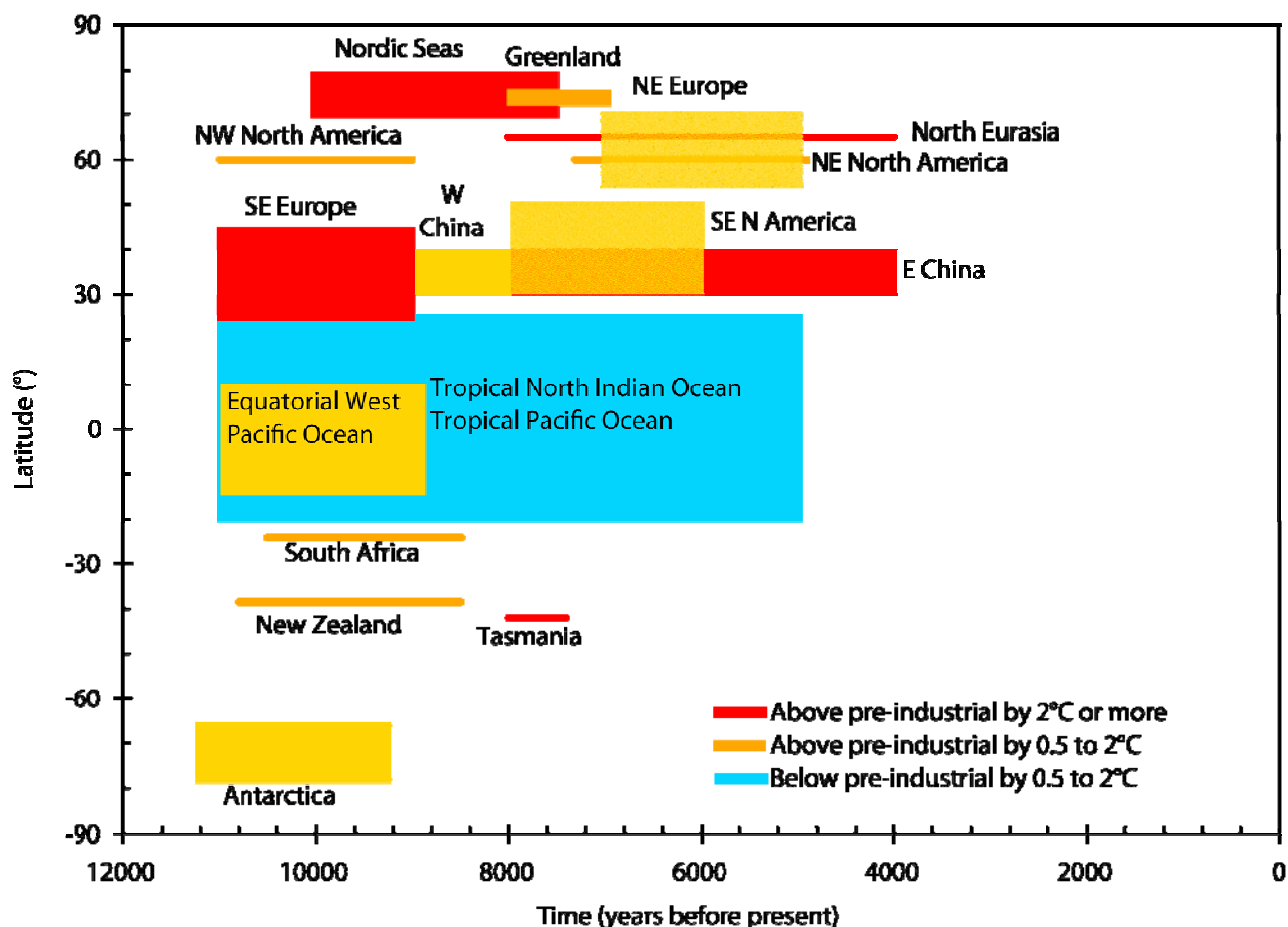
3
4
5 **Figure 6.9.** Timing and intensity of maximum temperature deviation from pre-industrial levels, as a function
6 of latitude (vertical axis) and time (horizontal axis, in thousands of years before present, 1950 A.D.).
7 Temperatures above pre-industrial levels by 0.5°C to 2°C appear in orange (above 2°C in red). Temperatures
8 below pre-industrial levels by 0.5°C to 2°C appear in blue. References for datasets are: Barents Sea
9 (Duplessy et al., 2001), Greenland (Johnsen et al., 2001), Europe (Davis et al., 2003), northwest and
10 northeast America (Kaufman et al., 2004; MacDonald et al., 2000), China (He et al., 2004), tropical oceans
11 (Rimbu et al., 2004; Stott et al., 2004; Lorentz et al., 2006), north Atlantic (Marchal et al., 2002; Kim et al.,
12 2004), Tasmania (Xia et al., 2001), East Antarctica (Masson et al., 2000), southern Africa (Holmgren et al.,
13 2003), New Zealand (Williams et al., 2004).
14

1
2
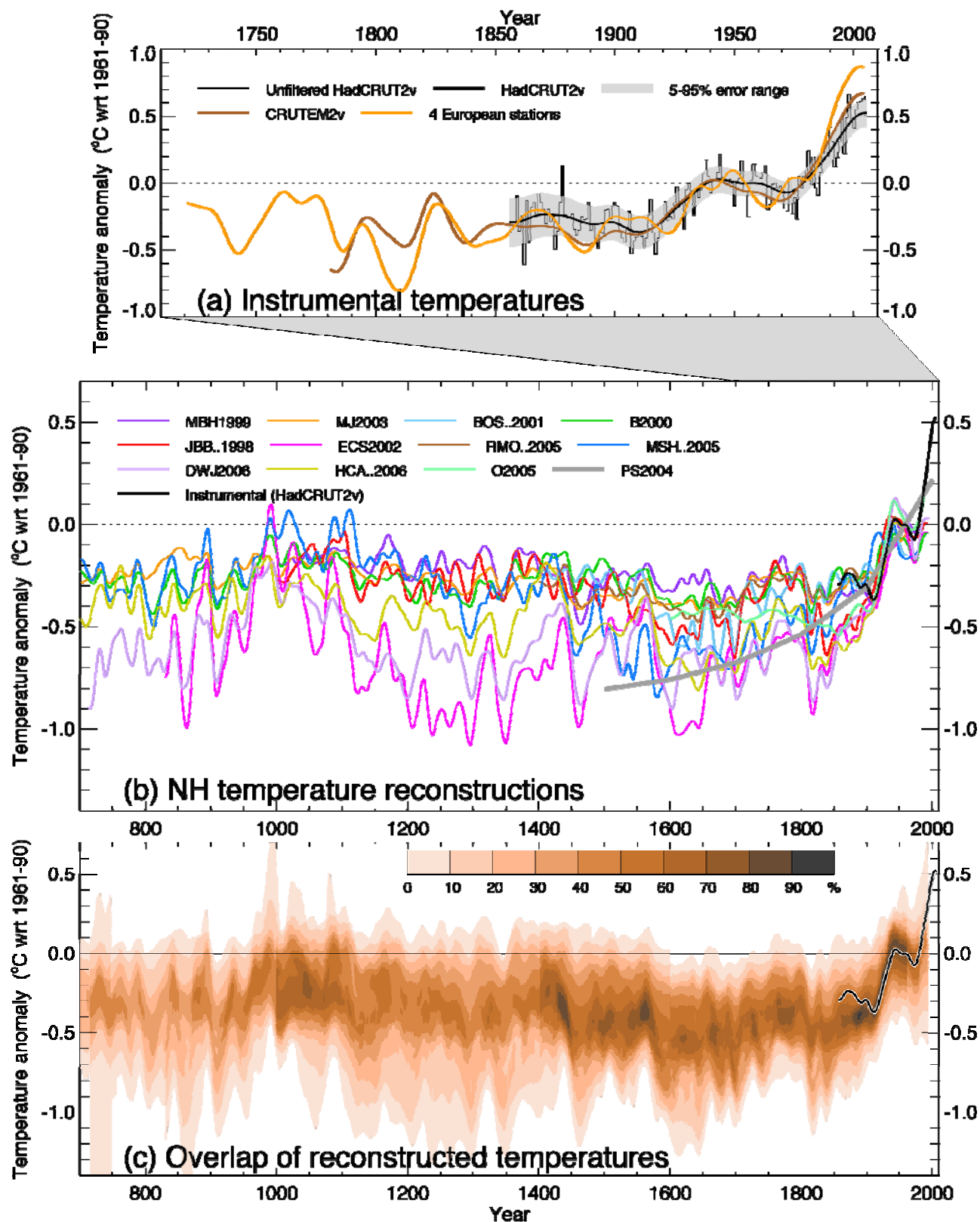
3
4
5 **Figure 6.10.** Records of Northern Hemisphere temperature variation during the last 1300 years. (a) Annual-
6 mean instrumental temperature records, identified in Table 6.1. (b) Reconstructions using multiple climate
7 proxy records, identified in Table 6.1, including three records (JBB..1998, MBH..1999, and BOS..2001)
8 shown in the TAR and the HadCRUT2v instrumental temperature record in black. (c) Overlap of the
9 published multi-decadal timescale uncertainty ranges of all temperature reconstructions identified in Table
10 6.1 (except for RMO...2005 and PS2004), with temperatures within ±1 standard error (SE) of a

1   reconstruction 'scoring' 10%, and regions within the 5–95% range 'scoring' 5% (the maximum 100% is
2   obtained only for temperatures that fall within ±1 SE of all 10 reconstructions). The HadCRUT2v
3   instrumental temperature record is shown in black. All series have been smoothed with a Gaussian-weighted
4   filter to remove fluctuations on time scales less than 30 years; smoothed values are obtained up to both ends
5   of each record by extending the records with the mean of the adjacent existing values. All temperatures
6   represent anomalies (°C) from the 1961–1990 mean.
7

1

(a) 1000

(b) 1500

(c) 1750

2
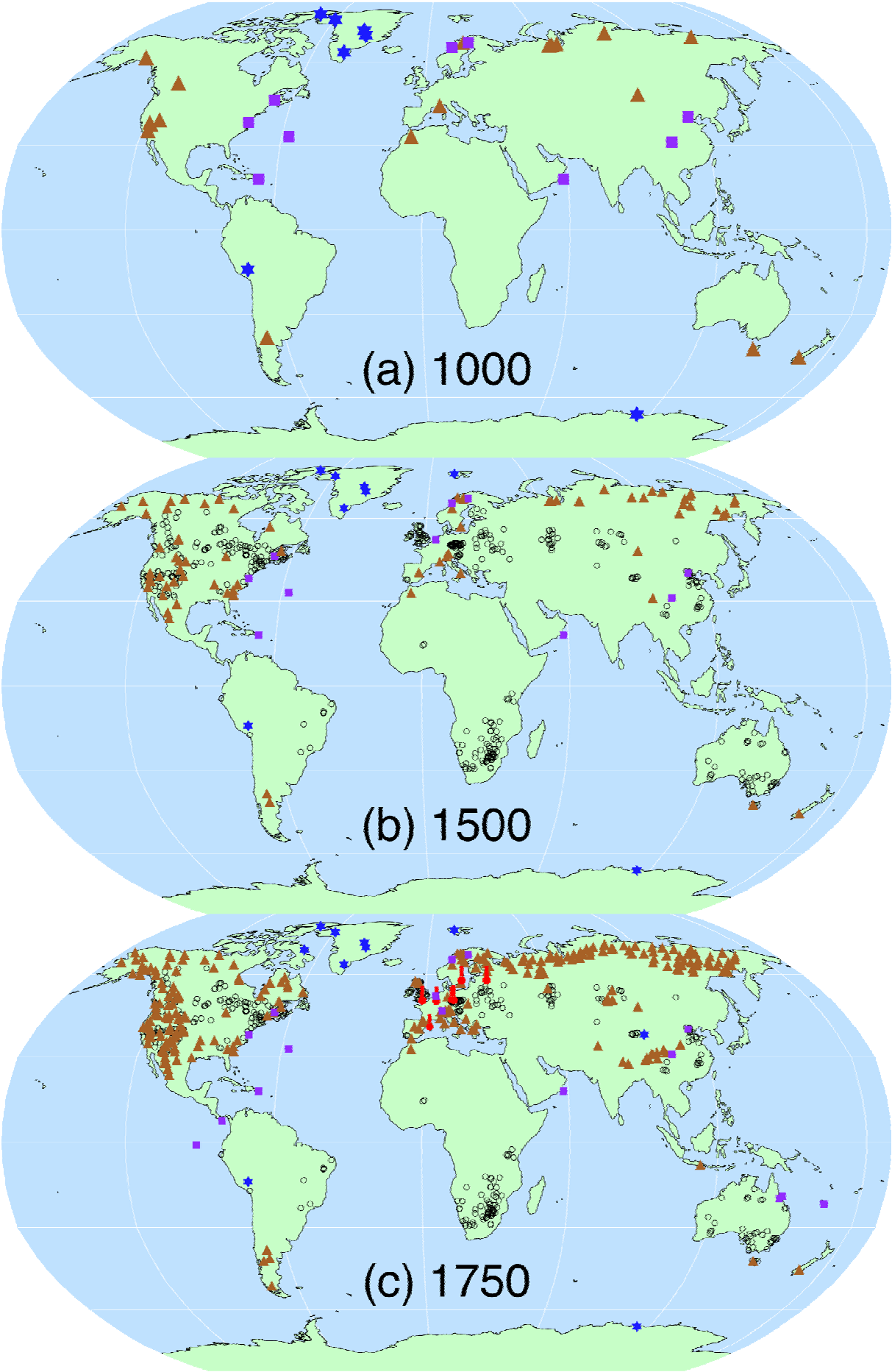
1   **Figure 6.11.** Locations of proxy records with data back to AD 1000, 1500 and 1750 (instrumental: red
2   thermometers; tree-ring: brown triangles; borehole: black circles; ice-core/ice-borehole: blue stars; other
3   including low-resolution records: purple squares) that have been used to reconstruct Northern or Southern
4   Hemisphere temperatures by studies shown in Figure 6.10 (see Table 6.1, excluding O2005) or used to
5   indicate Southern Hemisphere regional temperatures (Figure 6.12).
6

1
2
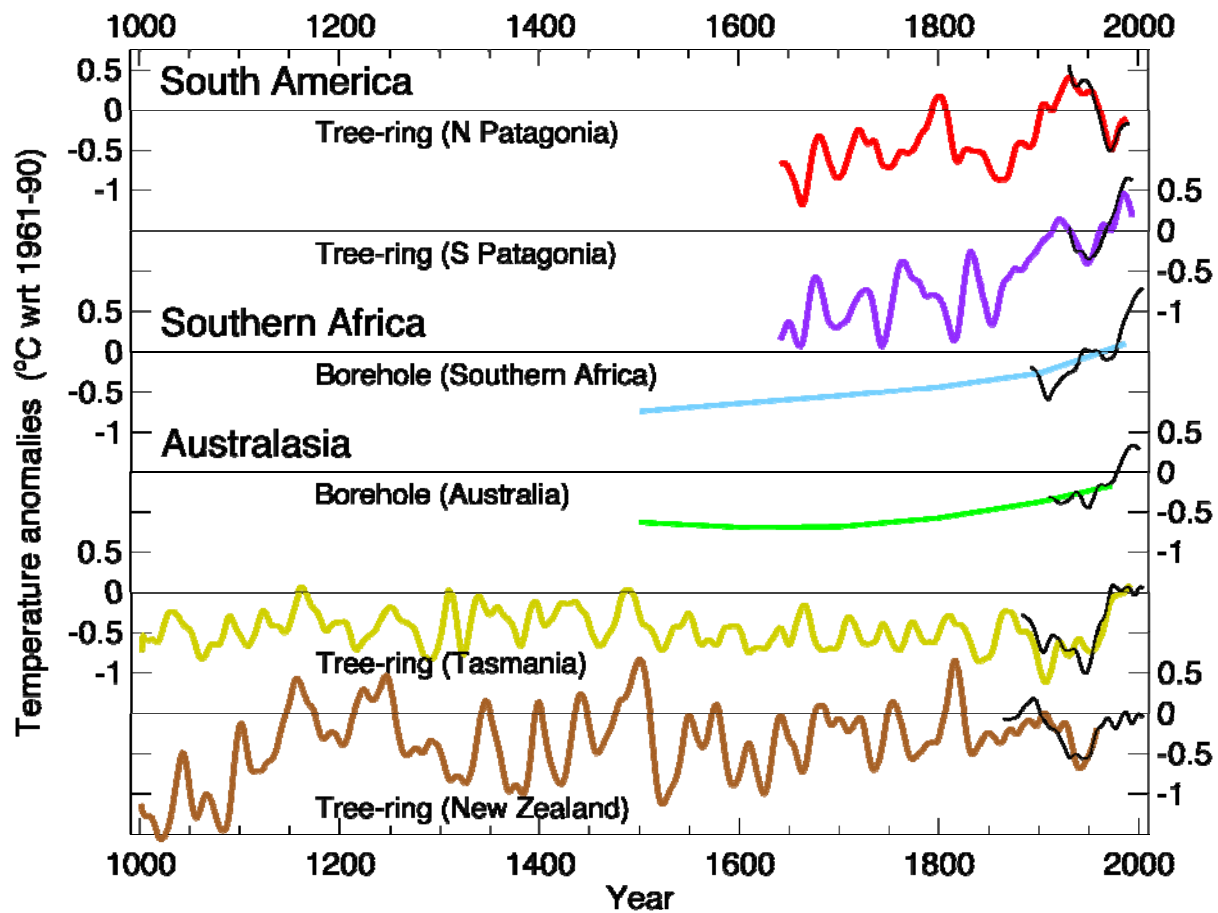
3
4
5 **Figure 6.12.** Temperature reconstructions for regions in the Southern Hemisphere: two annual temperature
6 series from South American tree-ring data (Villalba et al., 2003); annual temperature estimates from
7 borehole inversions for southern Africa and Australia (Huang et al, 2000); summer temperature series from
8 Tasmania and New Zealand tree-ring data (Cook et al., 2000; Cook et al., 2002a). The black curves show
9 summer or annual instrumental temperatures for each region. All tree-ring and instrumental series have been
10 smoothed with a 25-year filter and represent anomalies (°C) from the 1961–1990 mean (indicated by the
11 horizontal lines).
12

1
2
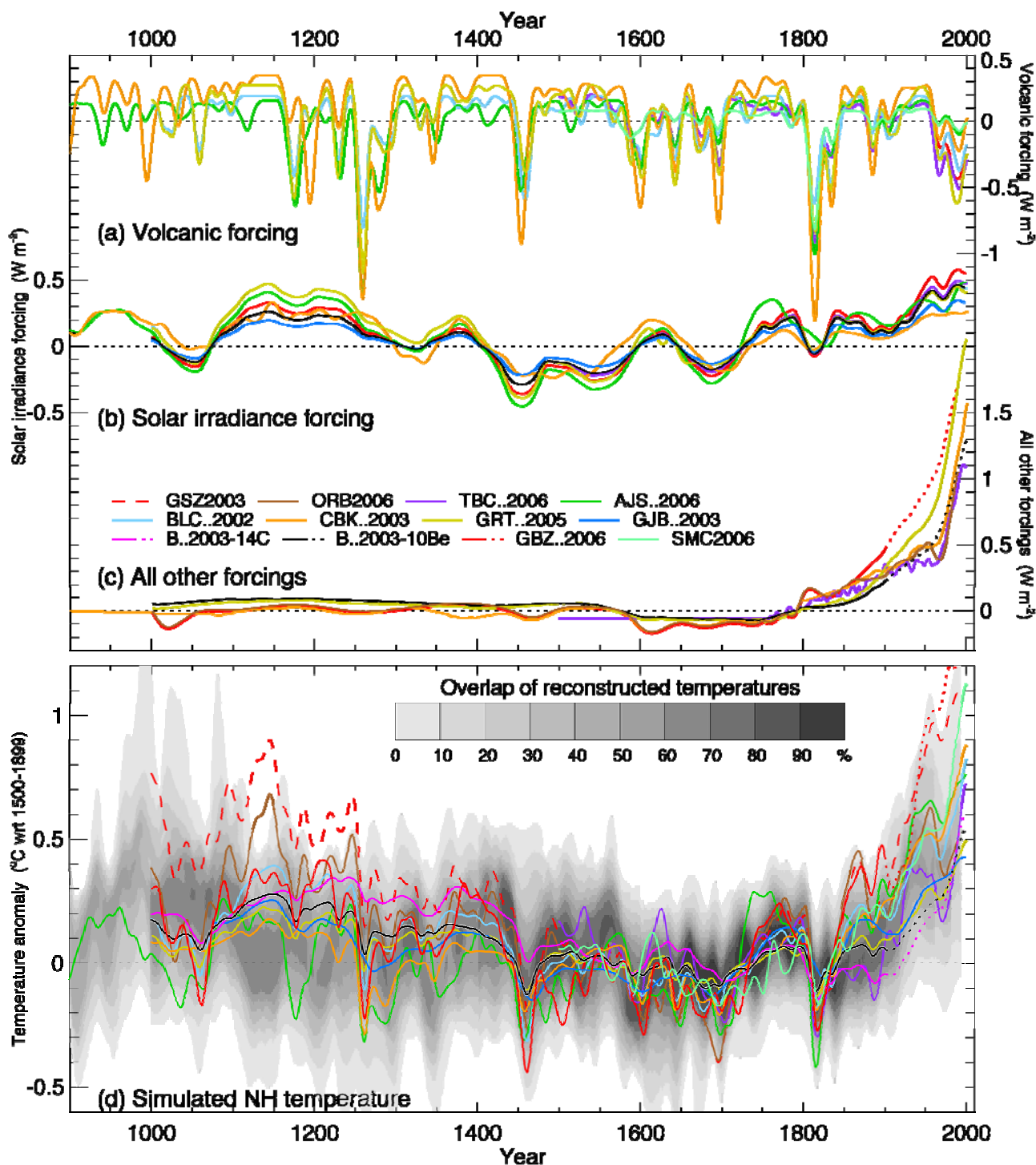
3
4
Figure 6.13. Radiative forcings and simulated temperatures during the last 1100 years. Global-mean
radiative forcing (W m^{-2}) used to drive climate model simulations due to (a) volcanic activity, (b) solar
irradiance variations, and (c) all other forcings (which vary between models, but always include greenhouse
gases, and, except for those with dotted lines after 1900, tropospheric sulphate aerosols). (d) Annual-mean
NH temperature (°C) simulated under the range of forcings shown in (a)-(c), compared with the
concentration of overlapping NH temperature reconstructions (shown by grey shading, modified from Figure
6.10c to account for the 1500–1899 reference period used here). All forcings and temperatures are expressed
as anomalies from their 1500–1899 means and then smoothed with a Gaussian-weighted filter to remove
fluctuations on time scales less than 30 years; smoothed values are obtained up to both ends of each record
by extending the records with the mean of the adjacent existing values. The individual series are identified in
Table 6.2.

1
2
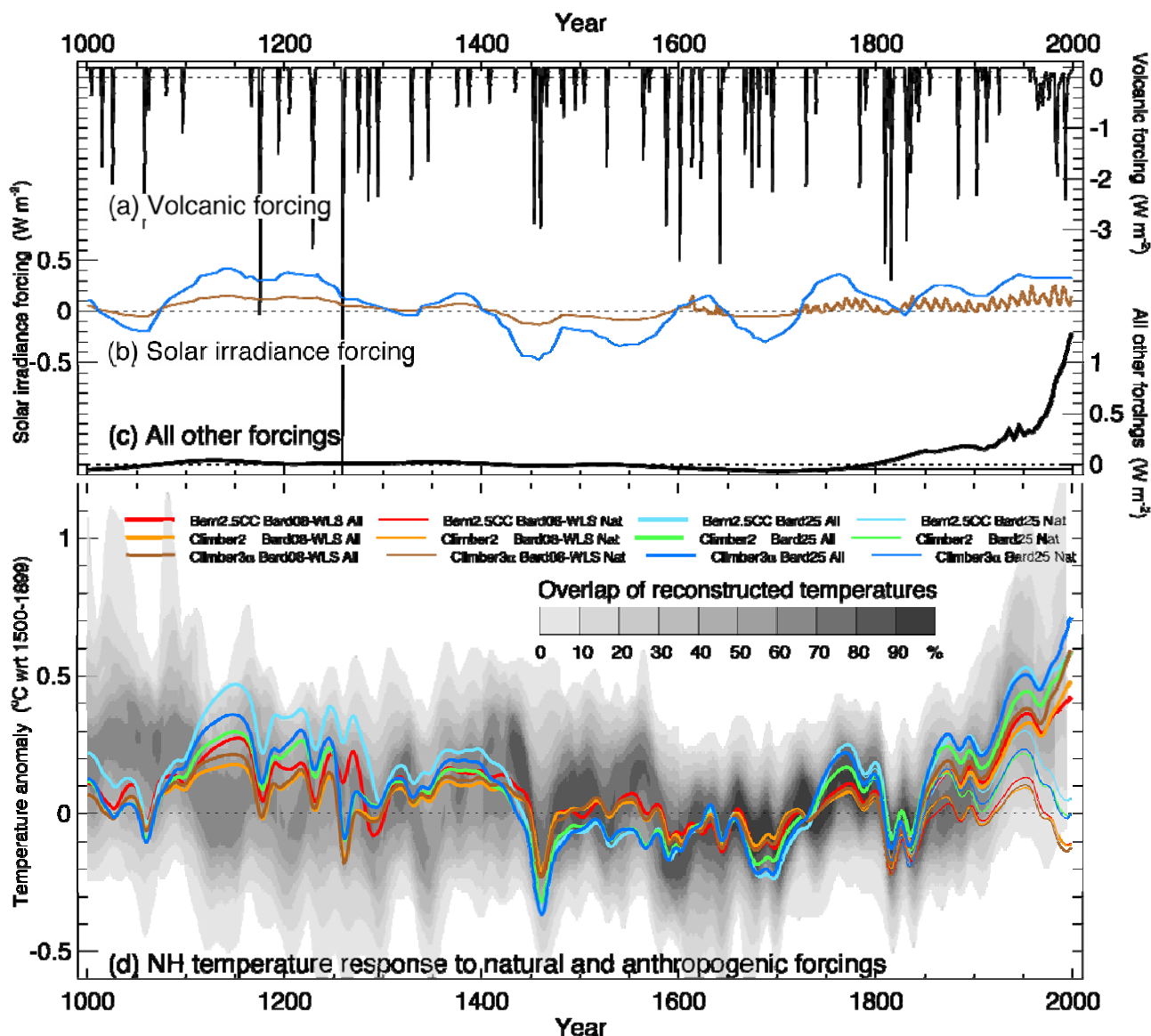
3
4 **Figure 6.14.** Simulated temperatures during the last 1000 years with and without anthropogenic forcing, and
5 also with weak or strong solar irradiance variations. Global-mean radiative forcing (W m^{-2}) used to drive
6 climate model simulations due to (a) volcanic activity, (b) strong (blue) and weak (brown) solar irradiance
7 variations, and (c) all other forcings, including greenhouse gases and tropospheric sulphate aerosols (the thin
8 flat line after 1765 indicates the fixed anthropogenic forcing using in the 'Nat' simulations). (d) Annual-
9 mean NH temperature (°C) simulated by three climate models under the forcings shown in (a)-(c), compared
10 with the concentration of overlapping NH temperature reconstructions (shown by grey shading, modified
11 from Figure 6.10c to account for the 1500–1899 reference period used here). 'All' [thick lines] used
12 anthropogenic and natural forcings, 'Nat' [thin lines] used only natural forcings. All forcings and
13 temperatures are expressed as anomalies from their 1500–1899 means; the temperatures were then smoothed
14 with a Gaussian-weighted filter to remove fluctuations on time scales less than 30 years. Note the different
15 vertical scale used for the volcanic forcing compared with the other forcings. The individual series are
16 identified in Table 6.3.
17

1
2
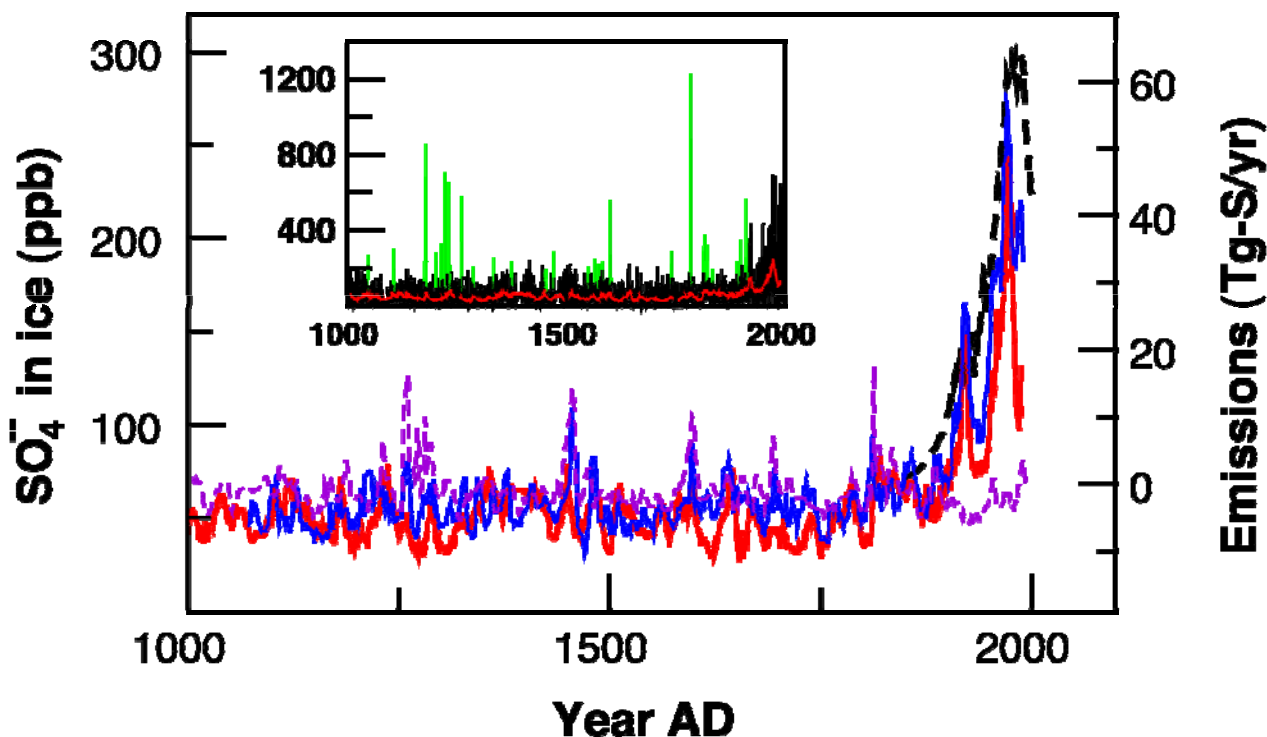
3
4
5 **Figure 6.15.** Sulfate concentrations in Greenland (Bigler et al., 2002, red line; Mieding, 2005, blue) and
6 Antarctic (Traufetter et al., 2004, dash, violet) ice cores during the last millennium. Also shown are the
7 estimated anthropogenic sulfur emissions for the Northern Hemisphere (Stern, 2005; dashed black). The ice
8 core data have been smoothed with a 10-year running median filter, thereby removing the peaks of major
9 volcanic eruptions. The inset illustrates the influence of volcanic emissions and shows monthly data as
10 measured (green), with identified volcanic spikes removed (black, most recent volcanic events were not
11 assigned nor removed), and results from the 10-year filter (red) (Bigler et al., 2002). The records represent
12 illustrative examples and can be influenced by local deposition events.
13

1
2
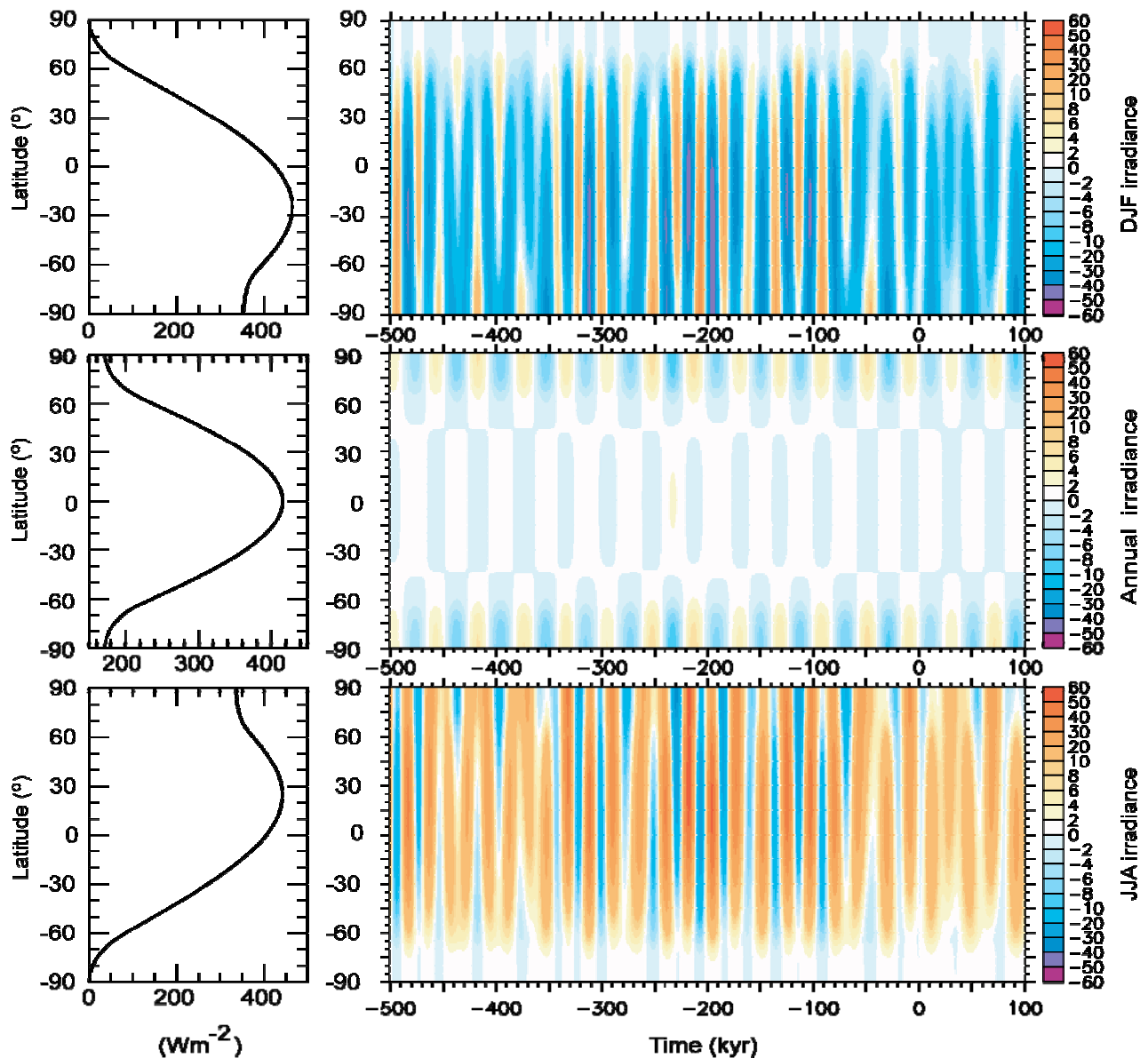
3
4
Box 6.1, Figure 1. December-January-February (top panel), annual mean (middle panel) and June-July-
August (bottom panel) latitudinal distribution of present-day (year 1950) incoming mean solar radiation (W
m^{-2}). Right side: deviations with respect to present-day of December-January-February (top panel), annual
mean (middle panel) and June-July-August (bottom panel) latitudinal distribution of incoming mean solar
radiation from the past 500 kyr to the future 100 kyr (W/m^{2}) (Berger and Loutre, 1991; Loutre et al., 2004).
10

1
2
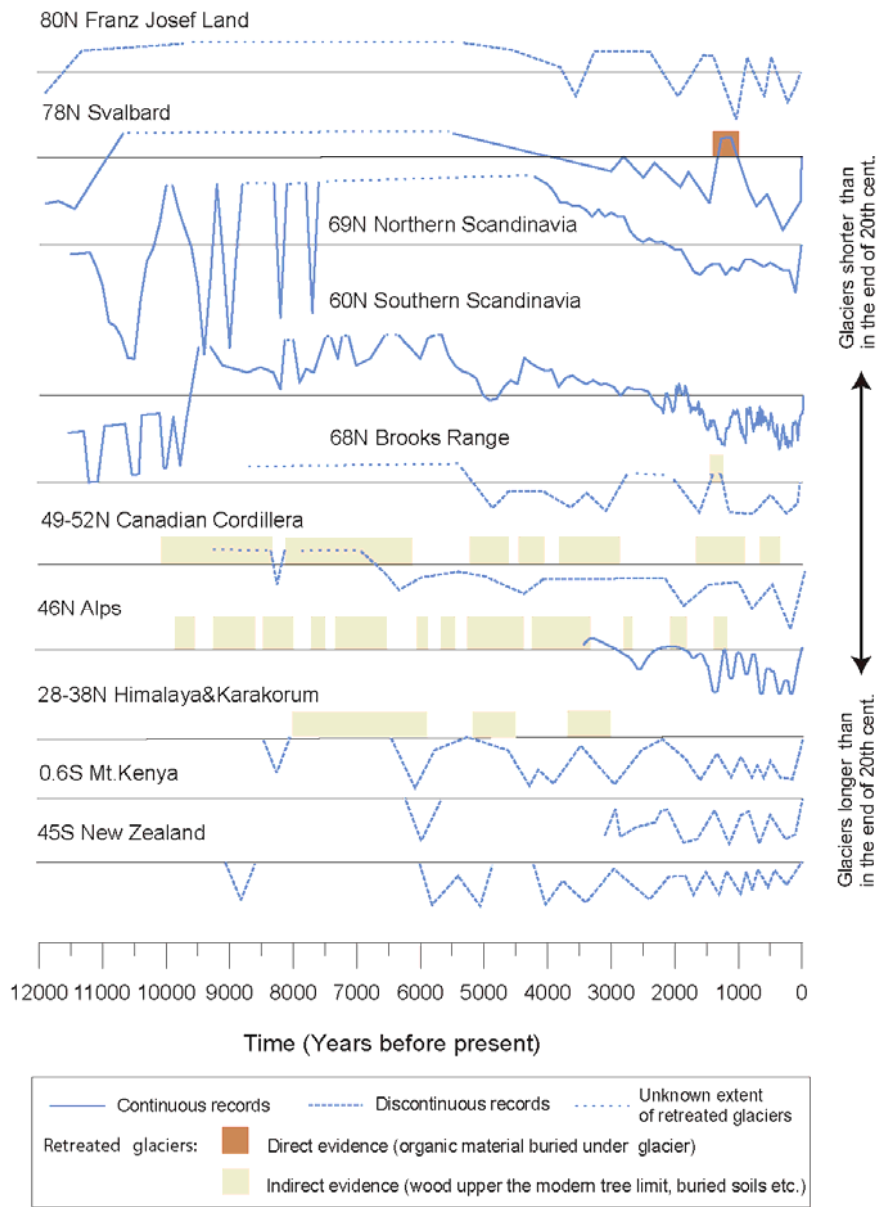
1 **Box 6.3, Figure 1.** Timing and relative scale of selected glacier records from both hemispheres. The
2 different records show that the Holocene glacier patterns are complex and that they should be interpreted
3 regionally in terms of precipitation and temperature. In most cases the scale of glacier retreat is unknown and
4 indicated - on a relative scale. Lines above the horizontal line indicate glaciers smaller than at the end of the
5 20th century and lines below the horizontal line denote periods with larger glaciers than at the end of the
6 20th century. The radiocarbon dates are calibrated and all curves are presented in calendar years. Franz Josef
7 Land (Lubinski et al., 1999), Svalbard – curve from (Svendsen and Mangerud, 1997) corrected with
8 (Humlum et al., 2005), Northern Scandinavia (Nesje et al., 2005; Bakke et al., 2005a, b), Southern
9 Scandinavia (Dahl and Nesje, 1996; Matthews et al., 2000, 2005; Lie et al., 2004), Brooks Range (Ellis and
10 Calkin, 1984), Canadian Cordillera (Luckman and Kearney, 1986; Osborn and Luckman, 1988; Koch et al.,
11 2004; Menounos et al., 2004), Alps (Holzhauser et al., 2005; Joerin et al., 2006), Himalaya and Karakorum –
12 (Röthlisberger and Geyh, 1985; Bao et al., 2003), Mt. Kenya (Karlen et al., 1999), New Zealand (Gellatly et
13 al., 1988).

1
2
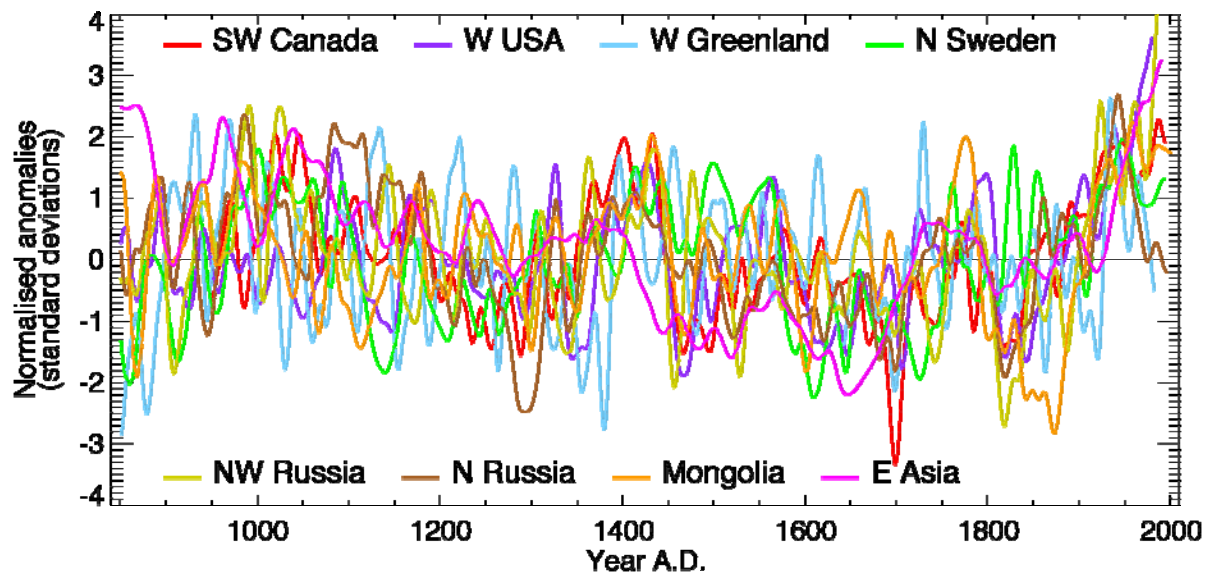
3
4
5
6 **Box 6.4, Figure 1.** The heterogeneous nature of climate during the "Medieval Warm Period" is illustrated by
7 the wide spread of values exhibited by the individual records that have been used to reconstruct NH-mean
8 temperature. Individual, or small regional averages of, proxy records collated from those used by Mann and
9 Jones (2003), Esper et al. (2002) and Luckman and Wilson (2005), but excluding shorter series or those with
10 no evidence of sensitivity to local temperature. These records have not been calibrated here, but each has
11 been smoothed with a 20-year filter and scaled to have zero mean and unit standard deviation over the period
12 1001–1980.
13

1
2
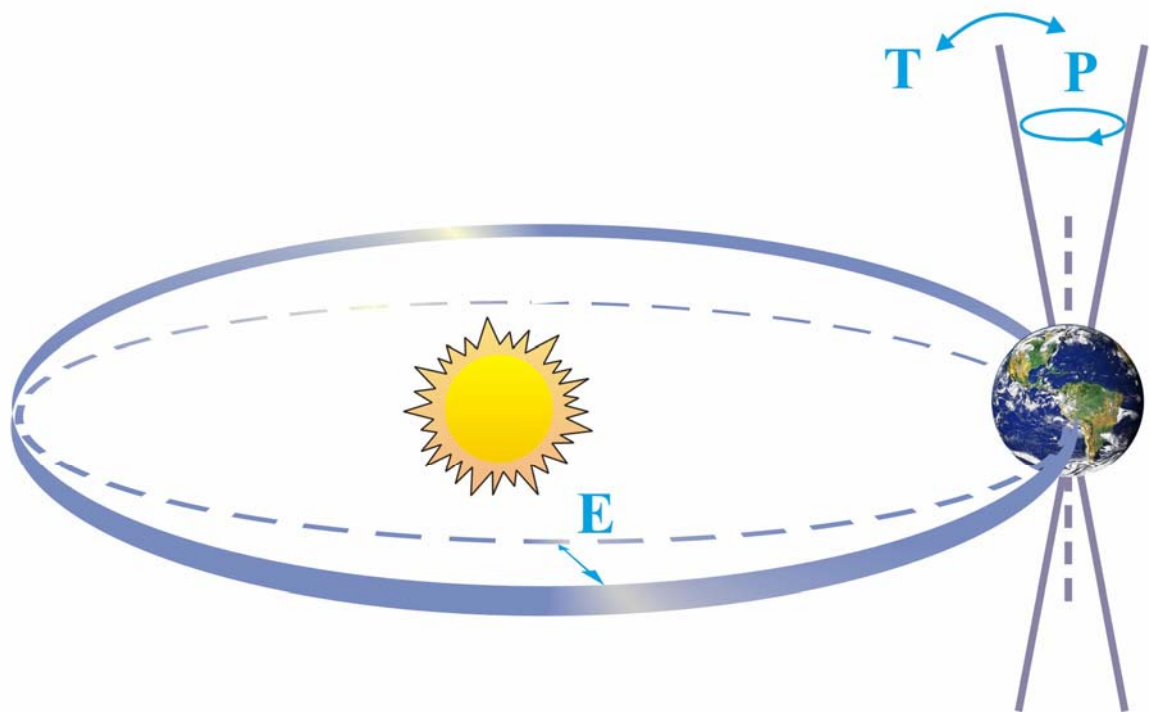
3
4
5 **FAQ 6.1, Figure 1.** Schematic of the Earth's orbital changes (Milankovich cycles) that drive the ice age
6 cycles. "T" denotes changes in the tilt (or obliquity) of the Earth axis, "E" denotes changes in the eccentricity
7 of the orbit (due to variations in the minor axis of the ellipse), and "P" denotes precession, i.e., changes in the
8 direction of the axis tilt at a given point of the orbit. Source: Rahmstorf and Schellnhuber (2006).
9
10
11